



Cite this: *Chem. Commun.*, 2017, **53**, 10882

Received 12th February 2017,  
Accepted 13th June 2017

DOI: 10.1039/c7cc01104k

rsc.li/chemcomm

# An annealing-free aqueous-processed anatase TiO<sub>2</sub> compact layer for efficient planar heterojunction perovskite solar cells†

Chengwu Yang,<sup>a</sup> Mingyu Yu,<sup>a</sup> Dichun Chen,<sup>b</sup> Yaqing Zhou,<sup>a</sup> Wei Wang,<sup>a</sup> Yang Li,<sup>a</sup> Tung-Chun Lee <sup>\*c</sup> and Daqin Yun<sup>\*a</sup>

**A facile aqueous-based fabrication scheme is developed for producing annealing-free anatase TiO<sub>2</sub> (AF-TiO<sub>2</sub>) films that exhibit efficient electron transport properties in planar heterojunction perovskite solar cells (PSCs). AF-TiO<sub>2</sub> films are fabricated by spin coating on a substrate a colloidal solution of anatase TiO<sub>2</sub> nanoparticles (NPs) prepared *via* a low temperature hydrolytic sol–gel method. The resultant AF-TiO<sub>2</sub> films show low electrical resistance, high transmittance in the visible and near-infrared regions and facilitation of high-quality perovskite film formation, which can be attributed to their homogeneous surface morphology and nanocrystallinity. The AF-TiO<sub>2</sub> based PSCs achieve a power conversion efficiency (PCE) of 18.29 ± 0.18%, showing significant improvement compared to the control PSCs (PCE = 11.33 ± 0.32%) based on TiO<sub>2</sub> films made by high-temperature annealing of amorphous TiO<sub>2</sub> (HTA-TiO<sub>2</sub>).**

Solution-processable perovskite solar cells (PSCs) have recently attracted significant attention as a promising candidate for making high efficiency and flexible photovoltaic devices.<sup>1–6</sup> To date, numerous PSCs using TiO<sub>2</sub> mesoporous structures have been shown to exhibit high power conversion efficiencies (PCEs) of over 20%.<sup>7–10</sup> However, mesoporous TiO<sub>2</sub> layers require a high-temperature annealing process (over 450 °C), which limits their use in flexible PSCs. As an alternative to mesoporous TiO<sub>2</sub> PSCs, planar heterojunction (PHJ) PSCs made *via* low-temperature (< 150 °C) processing have been investigated extensively due to their simple device structures and their compatibility with flexible polymeric substrates as well as inverted device designs.<sup>11–14</sup> In general, the p–i–n type PHJ PSC structure consists of an electron transport layer (ETL), a perovskite absorber layer and a hole transport

layer (HTL). The ETL and HTL are responsible for extracting photo-generated charge carriers from the perovskite layer and transporting these carriers to the designated electrodes. Various types of materials have been employed in carrier transport layers, such as PEDOT:PSS, NiO<sub>x</sub>, CuSCN, poly(triaryl amine) (PTAA) and 2,2',7,7'-tetrakis-(*N,N*-di-*p*-methoxyphenylamine)-9,9'-spirobifluorene (Spiro-OMeTAD) as hole transport layers, and ZnO, SnO<sub>2</sub>, CsCO<sub>3</sub>, PCBM and TiO<sub>2</sub> as electron transport layers.<sup>7,15–21</sup> Among these ETLs, TiO<sub>2</sub> is considered to be a promising electron transport material because of its environmentally friendly nature, wide band gap, high electron mobility and good stability.<sup>22–24</sup>

Recently, several vacuum deposition approaches have been developed for fabricating low-temperature processable TiO<sub>2</sub> ETLs for PHJ PSCs, such as atomic layer deposition,<sup>25</sup> electron-beam evaporation,<sup>26</sup> and magnetron sputtering.<sup>14</sup> Compared to vacuum methods, however, solution-based techniques are generally more cost-effective and scalable. Among them, sol–gel methods are arguably the most widely adopted routes for depositing TiO<sub>2</sub> films owing to ease in fabrication and low cost.<sup>4,11,27–29</sup> Nevertheless, the as-prepared TiO<sub>2</sub> films *via* the sol–gel methods are generally amorphous and therefore exhibit poor electrical conductivity, which incurs negative impacts on the performance of PSCs.<sup>11,30</sup> Strategies have been developed to enhance the electrical properties of TiO<sub>2</sub> films *via* optimising their morphology, doping and composition; these strategies include surface modification of TiO<sub>2</sub> with TiCl<sub>4</sub> treatment, ozone (O<sub>3</sub>) treatment,<sup>31,32</sup> and doping modification of the TiO<sub>2</sub> film with an appropriate substitution of Li<sup>+</sup>, Mg<sup>2+</sup>, Al<sup>3+</sup>, Y<sup>3+</sup>, and Nb<sup>5+</sup>.<sup>4,18,33–35</sup> In particular, the formation of crystalline TiO<sub>2</sub> at a low temperature is considered to be one of the most direct and efficient strategies to improve the electrical characteristics for highly efficient PSCs.<sup>29,30</sup> In this context, considerable effort has been devoted to prepare TiO<sub>2</sub> nanocrystals (NCs) through a low-temperature non-hydrolytic sol–gel method for PSC applications.<sup>16,32,36</sup> However, it remains a challenge to synthesise high-quality anatase TiO<sub>2</sub> NCs *via* the low-temperature hydrolytic sol–gel method for efficient PSCs.

Herein, we report a facile, efficient and environmentally friendly approach for preparing ultrathin anatase TiO<sub>2</sub> films

<sup>a</sup> College of Energy, Xiamen University, Xiamen 361002, China.

E-mail: dqyun@xmu.edu.cn

<sup>b</sup> Xiamen Branch of Luoyang Ship Material Research Institute, Xiamen, 361006, China

<sup>c</sup> Department of Chemistry and Institute for Materials Discovery, University College London (UCL), UK. E-mail: tungchun.lee@ucl.ac.uk

† Electronic supplementary information (ESI) available: Experimental details including synthesis, experimental procedure and supporting data. See DOI: 10.1039/c7cc01104k



*via* an aqueous-based and annealing-free fabrication scheme. The resultant annealing-free anatase TiO<sub>2</sub> (AF-TiO<sub>2</sub>) films can act as an efficient electron transport layer for planar heterojunction PSCs. The nanocrystalline anatase TiO<sub>2</sub> nanoparticles (NPs) prepared by this low-temperature hydrolytic sol-gel method can form stable nanocolloidal solutions in aqueous media, enabling the preparation of a smooth film with high optical transmittance. The resultant AF-TiO<sub>2</sub> film shows better electron extraction ability than that of the conventional TiO<sub>2</sub> films prepared in organic solvents and treated *via* high-temperature annealing processes, abbreviated as HTA-TiO<sub>2</sub> below. Moreover, the AF-TiO<sub>2</sub> compact layer was also found to facilitate the formation of high-quality perovskite films.

A general drawback of the hydrolytic sol-gel method is the amorphous nature of the resultant TiO<sub>2</sub> NPs and thus the requirement of a post-synthetic high-temperature (over 450 °C) annealing step to induce crystallisation. In our case, the low-temperature hydrolysis of titanium(IV) isopropoxide (TTIP) is performed *via* a sol-gel method in the presence of HNO<sub>3</sub> as the hydrolysing agent, resulting in the formation of nanocrystalline anatase TiO<sub>2</sub> NPs (see the ESI† for detailed experimental procedures), consistent with other similar systems in the literature.<sup>37</sup> In this method, the fast initial nucleation step induces the formation of small electrostatically stabilised TiO<sub>2</sub> NPs. The subsequent ageing step at 80 °C triggers the formation of small nanocrystalline anatase domains within a TiO<sub>2</sub> NP. The mild reaction conditions (80 °C, 1 atmosphere pressure) and surfactant-free aqueous solvent systems make this method a promising way to produce high-quality anatase TiO<sub>2</sub> NPs for PSCs and other applications.

The as-synthesised anatase TiO<sub>2</sub> NPs can be readily dispersed in water to form nanocolloidal solutions that are stable for months (inset of Fig. 1a; concentration = 20 mg mL<sup>-1</sup>). Powder X-ray diffraction (XRD) measurements of this sample reveal typical diffraction peaks of anatase TiO<sub>2</sub> (Fig. 1a). In particular, the diffraction peaks centred at 25.40°, 38.28°, 47.46°, 54.26°, and 62.68° were assigned to (101), (004), (200), (105) and (204) diffractions, respectively. This result verifies that the as-synthesised TiO<sub>2</sub> NPs indeed contain a significant amount of the anatase domains. Scherrer peak width analysis<sup>22</sup> reveals the average size of the nanocrystalline domains to be approximately 6.1 nm. The inset of Fig. 1b shows a top-view scanning electron microscopy (SEM) image of an AF-TiO<sub>2</sub> film

on a glass/ITO substrate prepared by spin coating. It was observed that AF-TiO<sub>2</sub> can form a dense, pinhole-free, and uniform continuous film compared to that of HTA-TiO<sub>2</sub> (ESI,† Fig. S1). Additionally, the resultant AF-TiO<sub>2</sub> film shows good optical transparency, with transmittance greater than 85% in the entire visible region (Fig. 1b). For comparison, the effects of anatase TiO<sub>2</sub> film thicknesses on transmittance performance are shown in Fig. S2 (ESI†).

To gain further insights into the nanoscale morphology and nanocrystal structures, high-resolution transmission electron microscopy (HRTEM) has been performed. The HRTEM image (Fig. 2a) reveals that the TiO<sub>2</sub> NPs are around 15–25 nm in diameter. By analysing the diffraction-contrast image and the fast-Fourier transform FFT images of selected areas, individual crystal domains within a single NP are identified to have a domain size of 2.5–5.5 nm (Fig. 2b and c), consistent with that obtained by Scherrer peak width analysis. The selected area electron diffraction (SAED) pattern (Fig. 2a, inset) displayed typical electron diffraction rings corresponding to the (101), (004), (200), and (105) lattice planes of the anatase structure of TiO<sub>2</sub>, consistent with the powder XRD results (Fig. 1a). These results indicate that the TiO<sub>2</sub> NPs indeed contain a high proportion of nanocrystalline anatase phase, implying that they have a reduced number of surface defect traps and could therefore enhance charge extraction on the interface between the TiO<sub>2</sub> layer and the perovskite layer.

To investigate the performance of the AF-TiO<sub>2</sub> films as ETLs in PHJ PSCs, a complete PSC device has been fabricated. A cross-sectional SEM image of a typical device architecture is shown in Fig. 3a. The electrodes of indium tin oxide (ITO) and Ag were used as the bottom cathode and the top anode, respectively. The thicknesses of the ETL (TiO<sub>2</sub>), the HTL (Spiro-OMeTAD) and the (FAPbI<sub>3</sub>)<sub>x</sub>(MAPbCl<sub>3</sub>)<sub>1-x</sub> perovskite absorber layer are approximately 60 nm, 260 nm, and 600 nm, respectively. It is noted that the smooth morphology of the AF-TiO<sub>2</sub> films can facilitate the

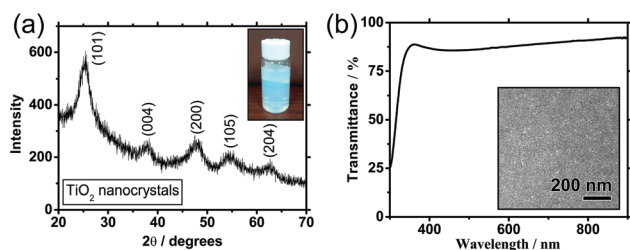


**Fig. 1** (a) Powder X-ray diffraction pattern of AF-TiO<sub>2</sub> nanoparticles. Diffraction peaks of each crystal plane are labelled. (b) Transmittance spectra of AF-TiO<sub>2</sub> films deposited on a glass substrate. The inset shows a representative SEM image of AF-TiO<sub>2</sub> deposited on a glass/ITO substrate, exhibiting a smooth morphology.

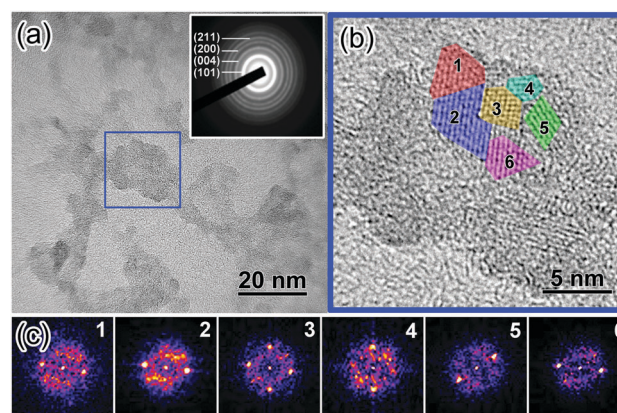


**Fig. 2** (a) Bright-field HRTEM image of TiO<sub>2</sub> nanocrystals deposited on a carbon film. The inset shows a selected area electron diffraction of TiO<sub>2</sub> NPs. Diffraction rings of the (101), (004), (200) and (105) planes are observed. (b) Zoom-in of the region of interest denoted by the blue square in (a). Selected adjacent nanocrystal domains are highlighted and numbered. Domain size: 2.5–5.5 nm. (c) FFT images of selected nanocrystal domains in (b), verifying the difference in crystal orientation.



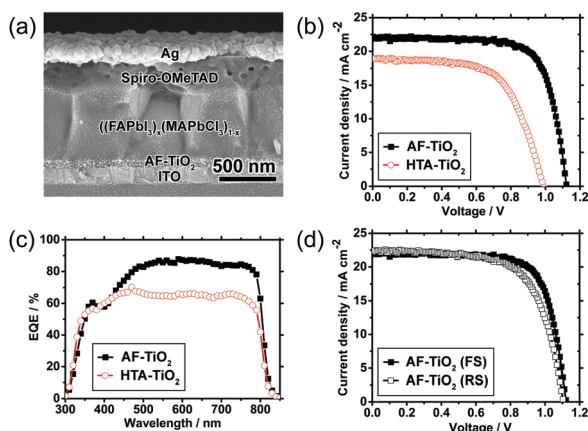


**Fig. 3** (a) Cross-sectional SEM image of a completed PSC device, with the structure of glass/ITO/TiO<sub>2</sub>/(FAPbI<sub>3</sub>)<sub>x</sub>(MAPbCl<sub>3</sub>)<sub>1-x</sub>/Spiro-OMeTAD/Ag. (b) *J*-*V* curves of typical devices using AF-TiO<sub>2</sub> and HTA-TiO<sub>2</sub> as ETLs. The measurements were performed under simulated AM 1.5 G sunlight (100 mW cm<sup>-2</sup>). (c) EQE spectra of representative devices comprising AF-TiO<sub>2</sub> and HTA-TiO<sub>2</sub> as ETLs. (d) Forward-scan (from 0 V to 1.2 V) and reverse-scan (from 1.2 V to 0 V) *J*-*V* curves of a typical AF-TiO<sub>2</sub> based device.

formation of highly crystalline and compact perovskite films (see Fig. S1, S3–S5, ESI† for details).

Fig. 3b shows the current-density-voltage (*J*-*V*) curves of the perovskite solar cells based on AF-TiO<sub>2</sub> compared to devices made of HTA-TiO<sub>2</sub>. The photovoltaic parameters of the devices are summarised in Table 1. Data in Table 1 show that the solar cell of HTA-TiO<sub>2</sub> exhibits considerably low short-circuit current density (*J*<sub>sc</sub>), open-circuit voltage (*V*<sub>oc</sub>), and fill factor (FF) values. In contrast, the overall PCE, including *J*<sub>sc</sub>, *V*<sub>oc</sub>, and FF, significantly increased when AF-TiO<sub>2</sub> NPs were used as the ETL. We propose that the notably high PCE of PSCs based on the AF-TiO<sub>2</sub> ETL is caused by the high content of the nanocrystalline anatase phase within the compact layer and the highly homogeneous morphology, which together favour electron extraction by reducing the rate of carrier recombination, compared to that of HTA-TiO<sub>2</sub>.<sup>11,21,32</sup> In particular, the dramatic difference in series resistance (*R*<sub>s</sub>) could be attributed to the presence of nanocrystalline TiO<sub>2</sub> domains that enhance electron transport, thereby improving the electrical characteristics.<sup>22</sup> As a result, the devices of AF-TiO<sub>2</sub> exhibit a *J*<sub>sc</sub> of 22.27 ± 0.19 mA cm<sup>-1</sup>, a *V*<sub>oc</sub> of 1.11 ± 0.01, and a FF of 73.63 ± 0.86%, corresponding to a PCE of 18.29 ± 0.18%, which shows significant improvement compared to that of control PSCs (PCE = 11.33 ± 0.32%) using HTA-TiO<sub>2</sub> films as the ETL. This result demonstrates that planar

structure photovoltaic devices based on AF-TiO<sub>2</sub> can indeed achieve a highly efficient power conversion, which sheds light on the development of highly efficient and flexible PSCs without relying on mesoporous TiO<sub>2</sub> structures.

Typical external quantum efficiency (EQE) data of the devices are shown in Fig. 3c. The integrated *J*<sub>sc</sub> values of the devices calculated from the EQE data were 21.63 mA cm<sup>-2</sup> and 17.45 mA cm<sup>-2</sup> for AF-TiO<sub>2</sub> and HTA-TiO<sub>2</sub>, respectively, which match well with the *J*-*V* measurement data (Table 1). The enhancement of EQE from 500 nm to 800 nm can be attributed to the smaller *R*<sub>s</sub> value and the improved morphology and crystallisation of the perovskite film facilitated by the AF-TiO<sub>2</sub> ETL (Fig. S1, S3–S5, ESI†).

The *J*-*V* curves and parameters of the AF-TiO<sub>2</sub> device measured for reverse and forward scan directions are shown in Fig. 3d and Table S2 (ESI†). Notably, the device does not exhibit distinct hysteresis, which is an indicator of inefficient charge transfer at the TiO<sub>2</sub>/perovskite interface, ferroelectric effects, ionic displacement and the trapping/detrapping of the charge carrier at the perovskite interface.<sup>38–41</sup> In an attempt to optimise the performance of TiO<sub>2</sub> ETLs, we have investigated the effects of the ETL thickness and that of the additional low-temperature annealing step after the deposition of anatase TiO<sub>2</sub> NPs by spin coating. Device-level measurement data based on 10 PSCs per configuration are presented in the ESI† (Fig. S2, S6–S12 and Tables S1–S4).

Electrical impedance spectroscopy (EIS) was performed to further study the interfacial charge transport properties of the PSCs.<sup>14,42</sup> Nyquist plots of the devices were measured at a DC bias of 0–0.8 V in the dark and the equivalent circuit model for the perovskite solar cells is shown in Fig. 4a (see Fig. S12 (ESI†) for details). Compared to HTA-TiO<sub>2</sub>-based devices, the AF-TiO<sub>2</sub> based devices exhibit significantly smaller *R*<sub>s</sub> and larger recombination resistance (*R*<sub>rec</sub>), indicating more efficient extraction and transport of electrons at the AF-TiO<sub>2</sub>/perovskite interface, thus resulting in larger *J*<sub>sc</sub>, *V*<sub>oc</sub> and FF values for these solar cells.

In conclusion, we have developed a facile and environmentally friendly method for fabricating nanocrystalline anatase TiO<sub>2</sub> films as compact electron transport layers for PHJ PSCs. TiO<sub>2</sub> NPs with small (2.5–5.5 nm) anatase domains were successfully prepared *via* a low temperature hydrolytic sol-gel method. The aqueous TiO<sub>2</sub> nanocolloids can form *via* spin coating continuous thin films that show superior electron extraction capability and high optical transmittance and can facilitate the formation of high-quality perovskite films. The PSC based on AF-TiO<sub>2</sub> achieves a PCE of 18.29 ± 0.18%. This powerful and

**Table 1** Parameters of the PSCs, showing TiO<sub>2</sub> layer thickness, short-circuit current density (*J*<sub>sc</sub>), open-circuit voltage (*V*<sub>oc</sub>), fill factor (FF), power conversion efficiency (PCE) and series resistance (*R*<sub>s</sub>). Statistical analysis (average ± standard deviation) is based on measurements of 10 individual devices for both AF-TiO<sub>2</sub> and HTA-TiO<sub>2</sub> films. "Champion" refers to the measurement data of the device with the highest PCE

Compact layer (Annealing temperature)	Thickness <sup>a</sup> (nm)		<i>J</i> <sub>sc</sub> (mA cm <sup>-2</sup> )	<i>V</i> <sub>oc</sub> (V)	FF (%)	PCE (%)	<i>R</i> <sub>s</sub> (Ω cm <sup>2</sup> )
AF-TiO <sub>2</sub> (25 °C)	58 ± 2	Champion	22.41	1.10	74.87	18.50	4.49
		Average	22.27 ± 0.19	1.11 ± 0.01	73.63 ± 0.86	18.29 ± 0.18	4.79 ± 0.20
HTA-TiO <sub>2</sub> (500 °C)	61 ± 2	Champion	18.85	0.99	62.74	11.70	11.38
		Average	18.75 ± 0.11	0.98 ± 0.01	61.47 ± 1.44	11.33 ± 0.32	12.56 ± 1.34

<sup>a</sup> Thickness of the TiO<sub>2</sub> films was measured using a surface profilometer, consistent with the thickness determined by SEM.





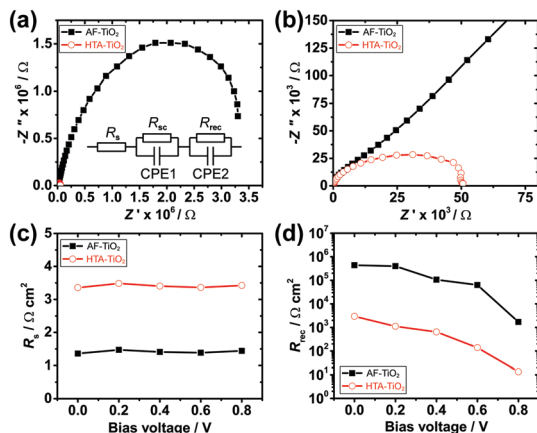


Fig. 4 (a) Nyquist plots of PSCs based on AF-TiO<sub>2</sub> and HTA-TiO<sub>2</sub> in the dark at a DC bias of 0 V. A 20 mV AC signal was applied with a frequency range of 0.01 Hz to 100 kHz. The inset shows the equivalent circuit adopted. (b) Nyquist plots of the high frequency region. (c)  $R_s$  as a function of bias. (d)  $R_{rec}$  as a function of bias.

generic strategy offers a novel way towards green, efficient and flexible PSC designs and beyond.

The research was funded by the Fundamental Research Funds for the Central Universities (2013121031) and the UCL BEAMS Future Leader Award through the EPSRC 2016 Institutional Sponsorship Award (EP/P511262/1). DY is grateful to the China Scholarship Council for funding. Nanfeng Zheng is acknowledged for his assistance in the IPCE measurements. Suyuan Xie is also gratefully acknowledged for his assistance in the  $J$ - $V$  characteristic measurements.

## Notes and references

- 1 A. Kojima, K. Teshima, Y. Shirai and T. Miyasaka, *J. Am. Chem. Soc.*, 2009, **131**, 6050–6051.
- 2 M. M. Lee, J. Teuscher, T. Miyasaka, T. N. Murakami and H. J. Snaith, *Science*, 2012, **338**, 643–647.
- 3 J. Burschka, N. Pellet, S. J. Moon, R. Humphry-Baker, P. Gao, M. K. Nazeeruddin and M. Grätzel, *Nature*, 2013, **499**, 316–319.
- 4 H. Zhou, Q. Chen, G. Li, S. Luo, T. B. Song, H. S. Duan, Z. Hong, J. You, Y. Liu and Y. Yang, *Science*, 2014, **345**, 542–546.
- 5 G. E. Eperon, S. D. Stranks, C. Menelaou, M. B. Johnston, L. M. Herz and H. J. Snaith, *Energy Environ. Sci.*, 2014, **7**, 982.
- 6 N. J. Jeon, J. H. Noh, W. S. Yang, Y. C. Kim, S. Ryu, J. Seo and S. I. Seok, *Nature*, 2015, **517**, 476–480.
- 7 W. S. Yang, J. H. Noh, N. J. Jeon, Y. C. Kim, S. Ryu, J. Seo and S. I. Seok, *Science*, 2015, **348**, 1234–1237.
- 8 D. Bi, W. Tress, M. I. Dar, P. Gao, J. Luo, C. Renevier, K. Schenk, A. Abate, F. Giordano and J.-P. C. Baena, *Sci. Adv.*, 2016, **2**, 1501170.
- 9 X. Li, D. Bi, C. Yi, J.-D. Décoppet, J. Luo, S. M. Zakeeruddin, A. Hagfeldt and M. Grätzel, *Science*, 2016, **353**, 58–62.
- 10 D. Bi, C. Yi, J. Luo, J.-D. Décoppet, F. Zhang, S. M. Zakeeruddin, X. Li, A. Hagfeldt and M. Grätzel, *Nat. Energy*, 2016, **1**, 16142.
- 11 B. Conings, L. Baeten, T. Jacobs, R. Dera, J. D'Haen, J. Manca and H. G. Boyen, *APL Mater.*, 2014, **2**, 081505.

- 12 C.-H. Chiang, Z.-L. Tseng and C.-G. Wu, *J. Mater. Chem. A*, 2014, **2**, 15897–15903.
- 13 Y. Li, L. Meng, Y. M. Yang, G. Xu, Z. Hong, Q. Chen, J. You, G. Li, Y. Yang and Y. Li, *Nat. Commun.*, 2016, **7**, 10214.
- 14 D. Yang, R. Yang, J. Zhang, Z. Yang, S. Liu and C. Li, *Energy Environ. Sci.*, 2015, **8**, 3208–3214.
- 15 D. Liu and T. L. Kelly, *Nat. Photonics*, 2013, **8**, 133–138.
- 16 H.-H. Wang, Q. Chen, H. Zhou, L. Song, Z. S. Louis, N. D. Marco, Y. Fang, P. Sun, T.-B. Song, H. Chen and Y. Yang, *J. Mater. Chem. A*, 2015, **3**, 9108–9115.
- 17 S. Ye, W. Sun, Y. Li, W. Yan, H. Peng, Z. Bian, Z. Liu and C. Huang, *Nano Lett.*, 2015, **15**, 3723–3728.
- 18 W. Chen, Y. Wu, Y. Yue, J. Liu, W. Zhang, X. Yang, H. Chen, E. Bi, I. Ashraful and M. Grätzel, *Science*, 2015, **350**, 944–948.
- 19 D. P. McMeekin, G. Sadoughi, W. Rehman, G. E. Eperon, M. Saliba, M. T. Hörantner, A. Haghighirad, N. Sakai, L. Korte and B. Rech, *Science*, 2016, **351**, 151–155.
- 20 Y. Wu, X. Yang, W. Chen, Y. Yue, M. Cai, F. Xie, E. Bi, A. Islam and L. Han, *Nat. Energy*, 2016, **1**, 16148.
- 21 Q. Jiang, L. Zhang, H. Wang, X. Yang, J. Meng, H. Liu, Z. Yin, J. Wu, X. Zhang and J. You, *Nat. Energy*, 2016, **2**, 16177.
- 22 K. Wojciechowski, M. Saliba, T. Leijtens, A. Abate and H. J. Snaith, *Energy Environ. Sci.*, 2014, **7**, 1142–1147.
- 23 D. Li, Y. Chen, P. Du, Z. Zhao, H. Zhao, Y. Ma and Z. Sun, *RSC Adv.*, 2015, **5**, 88973–88978.
- 24 Y. Zhao, Q. Zeng, X. Liu, S. Jiao, G. Pang, X. Du, K. Zhang and B. Yang, *J. Mater. Chem. A*, 2016, **4**, 11738–11746.
- 25 J. P. Correa Baena, L. Steier, W. Tress, M. Saliba, S. Neutzner, T. Matsui, F. Giordano, T. J. Jacobsson, A. R. Srimath Kandada, S. M. Zakeeruddin, A. Petrozza, A. Abate, M. K. Nazeeruddin, M. Grätzel and A. Hagfeldt, *Energy Environ. Sci.*, 2015, **8**, 2928–2934.
- 26 Y. Li, J. K. Cooper, W. Liu, C. M. Sutter-Fella, M. Amani, J. W. Beeman, A. Javey, J. W. Ager, Y. Liu, F. M. Toma and I. D. Sharp, *Nat. Commun.*, 2016, **7**, 12446.
- 27 M. Grätzel, *J. Sol-Gel Sci. Technol.*, 2001, **22**, 7–13.
- 28 L. Guo, C. Fei, R. Zhang, B. Li, T. Shen, J. Tian and G. Cao, *Sci. China Mater.*, 2016, **59**, 710–718.
- 29 G. Yang, H. Tao, P. Qin, W. Ke and G. Fang, *J. Mater. Chem. A*, 2016, **4**, 3970–3990.
- 30 A. Yella, L. P. Heiniger, P. Gao, M. K. Nazeeruddin and M. Grätzel, *Nano Lett.*, 2014, **14**, 2591–2596.
- 31 I. Jeong, H. Jung, M. Park, J. S. Park, H. J. Son, J. Joo, J. Lee and M. J. Ko, *Nano Energy*, 2016, **28**, 380–389.
- 32 Z. Liu, Q. Chen, Z. Hong, H. Zhou, X. Xu, N. De Marco, P. Sun, Z. Zhao, Y. B. Cheng and Y. Yang, *ACS Appl. Mater. Interfaces*, 2016, **8**, 11076–11083.
- 33 H. Zhang, J. Shi, X. Xu, L. Zhu, Y. Luo, D. Li and Q. Meng, *J. Mater. Chem. A*, 2016, **4**, 15383–15389.
- 34 Y. Bai, Q. Dong, Y. Shao, Y. Deng, Q. Wang, L. Shen, D. Wang, W. Wei and J. Huang, *Nat. Commun.*, 2016, **7**, 12806.
- 35 D. Liu, S. Li, P. Zhang, Y. Wang, R. Zhang, H. Sarvari, F. Wang, J. Wu, Z. Wang and Z. D. Chen, *Nano Energy*, 2017, **31**, 462–468.
- 36 N. D. Marco, H. Zhou, Q. Chen, P. Sun, Z. Liu, L. Meng, E.-P. Yao, Y. Liu, A. Schiffer and Y. Yang, *Nano Lett.*, 2016, **16**, 1009–1016.
- 37 G. Li, S. Zhang and J. Yu, *J. Am. Ceram. Soc.*, 2011, **94**, 4112–4115.
- 38 Y. Shao, Z. Xiao, C. Bi, Y. Yuan and J. Huang, *Nat. Commun.*, 2014, **5**, 5784.
- 39 W. Tress, N. Marinova, T. Moehl, S. Zakeeruddin, M. K. Nazeeruddin and M. Grätzel, *Energy Environ. Sci.*, 2015, **8**, 995–1004.
- 40 J. Wei, Y. Zhao, H. Li, G. Li, J. Pan, D. Xu, Q. Zhao and D. Yu, *J. Phys. Chem. Lett.*, 2014, **5**, 3937–3945.
- 41 J. M. Frost, K. T. Butler and A. Walsh, *APL Mater.*, 2014, **2**, 081506.
- 42 D. Liu, J. Yang and T. L. Kelly, *J. Am. Chem. Soc.*, 2014, **136**, 17116.

